View-angle-dependent AIRS cloudiness and radiance variance: Analysis and interpretation

Jie Gong[1] and Dong L. Wu[2]

[1] Upper tropospheric clouds play an important role in the global energy budget and hydrological cycle. Significant view-angle asymmetry has been observed in upper-level tropical clouds derived from 8 years of Atmospheric Infrared Sounder (AIRS) 15 μm radiances. Here we find that the asymmetry also exists in the extratropics. It is larger during day than that during night, more prominent near elevated terrain, and closely associated with deep convection and wind shear. The cloud radiance variance, a proxy for cloud inhomogeneity, has consistent characteristics of the asymmetry to those in the AIRS cloudiness. The leading causes of the view-dependent cloudiness asymmetry are the local time difference and small-scale organized cloud structures. The local time difference (1–1.5 h) of upper-level clouds between two AIRS outermost views can create parts of the observed asymmetry. On the other hand, small-scale tilted and banded structures of the upper-level clouds can induce about half of the observed view-angle-dependent differences in the AIRS cloud radiances and their variances. This estimate is inferred from analogous study using microwave humidity sounder radiances observed during the period of time when there were simultaneous measurements at two different view-angles from NOAA-18 and NOAA-19 satellites. The existence of tilted cloud structures and asymmetric 15 μm and 6.7 μm cloud radiances implies that cloud statistics would be view-angle-dependent, and should be taken into account in radiative transfer calculations, measurement uncertainty evaluations and cloud climatology investigations. In addition, the momentum forcing in the upper troposphere from tilted clouds is also likely asymmetric, which can affect atmospheric circulation anisotropically.

1. Introduction

[2] Cloud radiation feedback is known as one of the largest uncertainties in the prediction of future climate change [*Cess et al.*, 1990]. At the low and middle latitudes, the upper-troposphere clouds (e.g., anvils, cirrus clouds) associated with deep convection are of particular importance to the Earth's radiation budget [*Ramaswamy and Ramanathan*, 1989; *Su et al.*, 2009]. Parameters such as cloud optical depth, particle size and phase, and cloud top height are commonly used in cloud radiative forcing computation, but cloud three-dimensional effects are often ignored (e.g., the cloud top roughness). This simplification can induce significant errors [*Varnai and Marshak*, 2002]. For example, a rough cloud top will diffuse more shortwave radiation [*Kikuchi et al.*, 1994; *OÕHirok and Gautier*, 1998]. At the visible light spectrum, this effect leads to an effective "cloud albedo" [cf., *Diner et al.*, 1999]. Asymmetric infrared scattering by cloud particles is also often neglected in general circulation models (GCMs) and in remote sensing (e.g., outgoing long-wave radiation). The cloud long-wave radiation is considered isotropic, but more studies have pointed out such negligence could cause significant errors in radiation budget calculations [e.g., *Li and Fu*, 2000].

[3] Upper-level (UL) clouds are also part of the global hydrological cycle because of their impacts on precipitation and water vapor transport [*Cheng and Houze*, 1979]. *Ferrier et al.* [1996] found the tilted cloud structure is more important than ambient moisture in determining the precipitation efficiency. *Gu and Liou* [2006] showed that the precipitation rate was significantly sensitive to the inhomogeneity of ice water content of cirrus cloud in GCMs. A recent study by *Yuan et al.* [2011] with CloudSat radar measurements showed that tropical anvil structures could vary with particle phases and optical depth, but they did not discuss particle organization induced by dynamics.

[4] Momentum forcing carried by anvil clouds extended from cumulus convection can affect both new cloud development [*Zhang and Wu*, 2003] and atmospheric circulation [*Kang et al.*, 2010]. No GCMs currently take into account the direct momentum transport from tilted anvils or cirrus. The cumulus

[1]University Space Research Association, NASA Goddard Space Flight Center, Greenbelt, Maryland, USA.
[2]NASA Goddard Space Flight Center, Greenbelt, Maryland, USA.

Corresponding author: J. Gong, University Space Research Association, NASA Goddard Space Flight Center, Greenbelt, MD 20771, USA. (Jie.gong@nasa.gov)

momentum flux remains poorly represented in the state-of-art GCMs [*Arakawa*, 2004]. Hence, understanding and characterizing the impacts of UL clouds on radiation balance, hydrological cycle, and momentum budget requires more observational guidance about cloud internal properties.

[5] Passive satellite remote sensing instruments such as AIRS (Atmospheric Infrared Sounder), Microwave Limb Sounder have been routinely used for monitoring cloud systems from space [e.g., *Kahn et al.*, 2007; *Wu et al.*, 2005]. Wave clouds can be easily identified on satellite imagery but have rarely been analyzed, partly because two-dimensional infrared/visible images lack information about cloud vertical structures. At visible wavelengths, images that show cloud top roughness do not necessarily reveal cloud internal structures. Microwave channels, on the other hand, can penetrate through clouds, and probably have lower-level liquid cloud/precipitation/surface information blended in the signal. The IR sounding channels from AIRS and the Moderate Resolution Imaging Spectroradiometer are sensitive to the top 1–3 km layer of UL cloud vertical structures at relatively high spatial resolution (estimated from radiative transfer model). Unlike the Moderate Resolution Imaging Spectroradiometer broadband channels, AIRS hyperspectral radiances allow profiling cloud layers with the CO_2 and H_2O slicing technique as long as the radiances are not saturated by the cloud layer.

[6] Often associated with deep convection, UL clouds have a strong diurnal variation. The diurnal variation of tropical upper tropospheric clouds was studied extensively using the International Satellite Cloud Climatology Project (ISCCP) data set derived from the geostationary and polar orbiting satellites [*Wylie and Woolf*, 2002; *Yang and Slingo*, 2010] and precipitation radar such as Tropical Rainfall Measuring Mission (TRMM) [*Liu and Zipser*, 2008]. However, the ISCCP reported time-interval is too coarse (≥ 3 h) to capture rapid development of deep convection, especially during the early cloud development stage (typical lifecycle of deep convection is ~ 3 h). Tropical Rainfall Measuring Mission has very low sensitivity to upper-level anvils and cirrus [*Liu and Zipser*, 2008]. Furthermore, inconsistencies were found among various satellite measurements due to different viewing geometry [*Evan et al.*, 2007], which adds complexities to the cloud diurnal cycle problem. AIRS observations can be used to address the view-angle-dependent cloudiness, because each AIRS scan has 90 view angles that span $\pm 48.95°$ from the nadir. However, a relatively small range of local time ($1 - 1.5$ h) of these footprints must be taken into account when interpreting the angle-dependent differences.

[7] Cloud properties observed from space depend on viewing geometry of a particular instrument in several aspects, which can also affect cloud property retrievals [e.g., *Evan et al.*, 2007; *Maddux et al.*, 2010]. "Limb darkening" is one of the most known effects, in which the oblique view has a larger path length than the nadir view [*Lienesch and Wark*, 1967], causing its weighting function to peak at a slightly higher altitude, or, colder temperature in the troposphere. The difference between the pair of views that have the same angle will remove the "limb darkening" effect, and the remaining asymmetries are, in some cases, artifacts [e.g., *Buehler et al.*, 2005; *Campbell*, 2004; *Weng et al.*, 2003]. However, as a well-calibrated instrument [*Aumann et al.*, 2006], AIRS does not have view-dependent instrumental artifacts. Therefore, its view-angle-dependent radiances must convey real atmosphere information.

[8] *Gong and Wu* [2011] studied the view-angle-dependent AIRS cloud radiances in the tropics, and found significant asymmetry between AIRS west and east view angles. Tilted and banded cloud structures were thought as the main cause of the observed asymmetry, and the diurnal variation of clouds was neglected in that study. Here, these two hypotheses are further examined with AIRS radiances and other independent measurements. The contribution of the cloud diurnal variation is not negligible, whereas the "tilted and banded structure" cloud can explain at least half of the observed features.

[9] The rest of the paper is organized as follows. We will first briefly describe the AIRS instrument and the analysis method. The observations of AIRS view-angle-dependent asymmetry in cloud count and variance will be presented in section 3. Microwave Humidity Sounder (MHS) radiances are analyzed to evaluate the view-angle effect. Interpretation of the observed asymmetry is given in section 4, along with discussions on the possible causes and relative importance of the diurnal variation and the banded cloud structures. Section 5 is the conclusion.

2. Instrument and Method

2.1. AIRS Instrument and Sampling

[10] Launched in April 2002, AIRS is a hyperspectral spectrometer and sounder that measures Earth atmosphere thermal emissions in three infrared bands (3.75–4.61 μm, 6.20–8.22 μm, and 8.80–15.40 μm). AIRS makes a 90-footprint cross-track scan every 8/3 s with a nadir footprint size of 13.5 km and a swath width of 1650 km. AIRS scans are approximately along the zonal direction at low and middle latitudes (the scan intercepts the equator at an angle of $\sim 8°$).

[11] Aqua AIRS is on a Sun-synchronous polar orbit with fixed local solar times (LST, 1:30 and 13:30) at the equator crossing. The 1650 km swath width creates a local time difference (LTD) among different view-angles (Figure 1). The LTD is about 1 h between the outermost two views at the tropics, increases to ~ 1.5 h at 50° latitude. In this study, our analysis is limited to latitudes between 50°S and 50°N, where the scan direction is mostly in the east-west direction, and LST spans roughly between 1:00 A.M. (P.M.) to 2:00 A. M. (P.M.) within a scan, for ascending (descending) orbits.
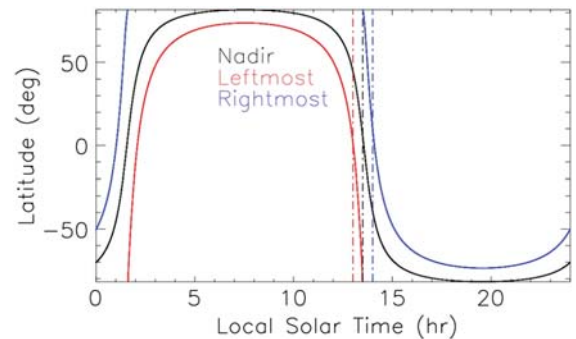
Figure 1. Local solar time for AIRS leftmost (red), nadir (black), and rightmost (blue) views when AIRS passes different latitudes.

[12] As in *Gong and Wu* [2011], AIRS Version 5 L1B 15 μm CO_2 radiances are used in the analysis. Other investigators [e.g., *McNally et al.*, 2006; *Kahn et al.*, 2007] also used these radiances to distinguish clouds at different height levels. In addition, this study includes several channels near 6.3 μm H_2O band, of which the weighting functions (WFs) peak between 300 and 650 hPa. Because water vapor has a steeper vertical gradient than CO_2, H_2O channels have better sensitivity to high clouds [*Soden and Bretherton*, 1993]. Moreover, they are not affected by the increasing CO_2 concentrations in time series. Cloud statistics are often consistent between CO_2 and H_2O radiances, and without losing generality, we only show cloud results from H_2O channels unless otherwise noted (all results shown in this paper are robust in both CO_2 and H_2O channels). The list of the selected channels with noise (NEdT) are given in Table A.1 in Error! Reference source not found.. AIRS L2/L3 cloud products are not suitable for this study because of their coarse resolution (50 km × 50 km) and because L3 products are unavailable at off-nadir views.

2.2. The Probability Density Function Cloud Detection Method

[13] The cloud detection procedure is summarized in Figure 2, which is the same as in *Gong and Wu* [2011]. First, we derive the radiance probability density function (PDF) for each view-angle, each channel (or pressure level), and at every 5° latitudinal bin, using a month's worth of data. The peak of the PDF is defined as the "clear-sky reference" (TB_{clr}, blue solid line in Figure 2), and any brightness temperature (T_B) that is lower than $TB_{clr} - 3\delta$ (bold black

dashed line) is considered as a robust cloud presence, where δ is the standard deviation estimated from the clear-sky portion of the PDF. The 3δ method has been proved to be a fast and effective way to screen-out cloud scenes, and has been applied in scientific research and many operational products [e.g., *Wu et al.*, 2005]. Cloud induced radiance depression is accordingly defined as $TB_C = TB - TB_{clr}$, where TB_C is always negative. There are three cloud categories, according to the coldness of TB_C: thin cloud, $(-3\delta > TB_C > -6\delta)$, medium thick cloud $(-6\delta > TB_C > -15\delta)$, and thick cloud $(TB_C < -15\delta)$. These classifications follow the same definitions as in *Gong and Wu* [2011]. Because infrared radiance cannot penetrate into optically thick clouds, AIRS is only capable of seeing the top 1–3 km of multilayer or thick clouds. Therefore, the three categories correspond roughly to cirrus, thick anvils and deep convective clouds, respectively. Using these thresholds, the number of clouds (CC) is counted for each category and for each view-angle. Cloud occurrence frequency is defined as the CC divided by the total number of samples at each view-angle bin.

[14] As shown in Figure 2, the limb-darkening effect is evident in AIRS radiances along the scan, which is symmetric about the nadir-view [*Minnis et al.*, 1991]. It can be described analytically by $TB_{clr}(\alpha) = TB_0 \ln[\cos(\alpha)]$, where TB_0 is the radiance at the nadir-view and α is the incident angle. The day and night $TB_{clr}(\alpha)$ are averaged and used to remove the limb-darkening effect before we apply cloud detection thresholds.

[15] Small-scale cloud structures (i.e., inhomogeneity), which can be seen in the radiance fluctuations within each AIRS scan, are estimated in terms of cloudy radiance variance (σ^2) using the deviation from 3-point running mean along the scan. The 3-point running window captures fluctuations with scales as small as ~ 50 km. The cloud/clear-sky variances are shown in Figure 2b, where colors represent different categories of cloud. In this particular case, although the medium thick cloud (purple) is much colder than other clouds detected along the scan, it is uniformly distributed, and the variance is hence smaller than the variance of the thin cloud (green).

[16] As in *Gong and Wu* [2011], we find the largest asymmetries at the outermost view-angles of medium thick clouds. The same definition for asymmetry factor is applied here, which is the difference between the average values of east and west views from 25° to 48.95° for the medium thick clouds ($\Delta X = X - \bar{X}$). The mean values of the same cloud type averaged over the same view-angle ranges are denoted by $\bar{X}$, where X can be CC (cloud count), σ^2 (cloud variance) and TB_C (cloud induced radiance depression).

2.3. Cloud Scale Analysis

[17] The 90 footprints along each AIRS scan possesses local time variations of cloud development within an hour. The linear regression line has a slight positive slope in AIRS cloudiness across the 90 footprints, which is not due to the view angle difference but likely due to the diurnal cycle. The variation of the rest of cloud statistics then may be considered due to cloud spatial/temporal variations. If the bulk statistics of clouds grow or decay linearly within one hour, we can retrieve the amplitude of cloud change rate using the 90 samples through regressing the slope of cloud
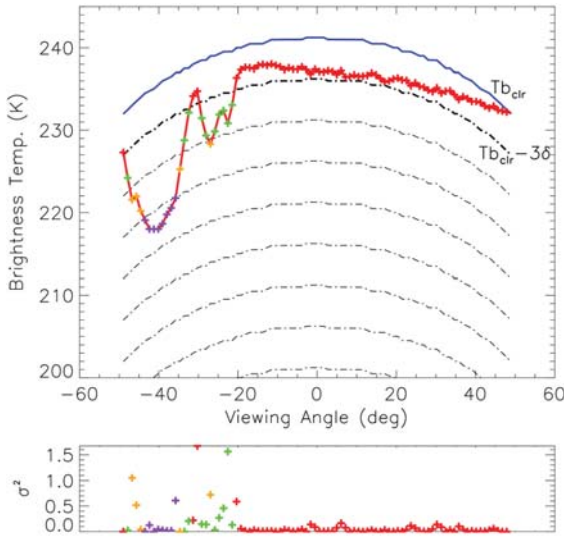
Figure 2. An example of AIRS radiance readings along one scan (a) and radiance variance due to different types of clouds (b). The colored symbols in Figure 2a denote the strength of cloud. Blue solid line is the clear-sky reference (TB_{clr}), and the black-dotted lines separate clouds into different categories according to their induced temperature depression. Each calculated radiance variance is tagged by the cloud strength color, with red (green) crosses from clear-sky (UL thin clouds), and orange and purple crosses from relatively thin and thick anvils, respectively.

occurrence frequency across the scan. Because AIRS does not sample the peak/trough hour of the diurnal cycle [*Wylie and Woolf*, 2002], the linear assumption is quite reasonable, and the absolute value of the slope is proportional to the amplitude of the cloud diurnal cycle within the AIRS passing hour. Besides the slow component of cloud variations, mesoscale/subhour cloud varies in the 90 cross-scan samples. Depending on whether the variability is interpreted as spatial or temporal change, the small-scale fluctuations correspond to spatial scale less than 1650 km (spatially) or period less than 1 h (temporally). The decomposition process can be summarized in equation (1).

$$F(x) = Ax + B + \frac{1}{90}\sum_{i=1}^{90-1} C_i e^{-2\pi i x} \tag{1}$$

[18] F is either the cloud count or cloud variance, where the angle symmetric dependency caused by "limb-darkening" effect has been preremoved as described in section 2.2. x is either sample distance (L) or local time (t). A (B) is the "amplitude" (mean) of a larger/longer scale variation (e.g., diurnal cycle). The third term on the right-hand side is a Fourier decomposition, where the spatial scale (or period) corresponding to the maximum value of $|C_i|$ is considered as the dominant spatial scale (or period) of the smaller-scale (or higher-frequency) signals. The physical meaning of this term is going to be elaborated in section 4.3.

## 2.4. Aliasing Between Temporal and Spatial Variations

[19] The cloud variability across the 90 footprints becomes difficult to interpret when cloud structures (tilted and banded) and temporal variations (e.g., the diurnal cycle) are both important. To isolate effects of cloud diurnal variations, we analyze radiance data from the MHS onboard NOAA-18 and NOAA-19 satellites that were sampled at the same local time but at different view angles. Because the two satellites are precessing slowly, in August 2011, the 37° west-view of NOAA-18 and the 37° east-view of NOAA-19 have the same local time at the equator, corresponding to 13.9 (1.9) LST for the ascending (descending) orbits (Figure 3). Thus, the LTD contributions in this case are assumed minimal. Assuming random sampling of a cloud ensemble during this month, differences in cloud statistics between the two MHS data sets near the paired 37° view angles are primarily due to the viewing geometry. For the MHS data, we use Channel 3 (183±1 Hz) L1B radiances, which has the weighting function most similar to AIRS 400 hPa channels with peaks in the upper-middle troposphere.

3. Cloud Amount and Variance Asymmetries

3.1. AIRS Cloud Radiance Asymmetry

[20] The observed statistics of AIRS cloud radiances are asymmetric about nadir between paired east-west views. This asymmetry exists globally in both cloud count and cloud variance statistics.

[21] To quantify this asymmetry, we compute 8 year cloud statistics from AIRS radiance data, and directly compare the PDFs from the paired east and west views. These PDFs are normalized such that their integral is unity. As shown in Figure 4, the January PDFs of 400 hPa H_2O channel radiances at the equator between east and west views are
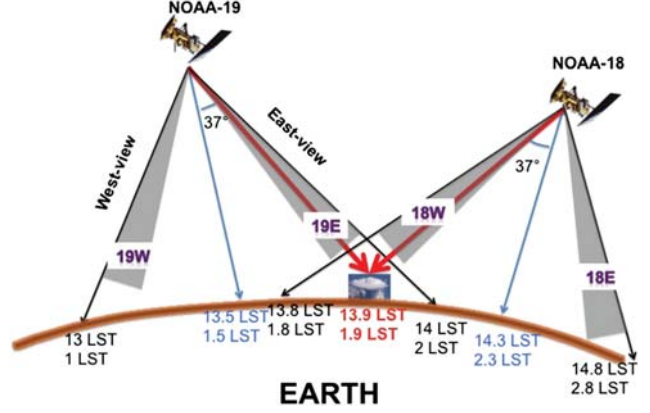

Figure 3. A diagram showing the viewing geometry of MHS onboard NOAA-18 and NOAA-19 during August, 2011.

significantly different for day against night (the negative FOV values always correspond to the west-view throughout this paper). Figure 4c is the day versus night PDF difference, and Figure 4d shows the mean PDF (day + night) as a function of view-angle. The 3δ lines (purple) used to separate the clear-sky and clouds from west and east views overlap with each other, indicating that the clear-sky asymmetry is negligible. The differences of the cloud PDFs in Figures 4a and 4b are generally negative, meaning that AIRS west-views observe a less amount of clouds than the east-views. The negative cloud PDF difference is found larger in the local noon than in the local midnight in almost all view-angles despite some fluctuations. There is a signature in Figure 4a that the PDF disparity becomes larger in percentage at colder cloud TB_C. The day-night contrast has larger magnitudes than the west-east view difference. In the $TB_{clr} \pm 3\delta$ bin, this is mainly due to the shift of the PDF curve as the nighttime TB is cooler than daytime (i.e., the shift of the TB_{clr} line). In the $< TB_{clr} - 3\delta$ bin (cloudy case), the day time PDFs exhibit a higher probability, which likely has a contribution from cloud diurnal variations. Although H_2O channels are sensitive to water vapor distributions as well, the fact that we saw extremely similar features from comparable CO_2 channels (not shown) confirm that the majority of the observed asymmetry comes from cloud instead of water vapor.

[22] Studying the AIRS cloud amount dependence on view-angle and radiance, *Gong and Wu* [2011] found that the largest asymmetry was associated with the medium thick clouds at the outermost views. Using the same method as in *Gong and Wu* [2011], we calculate the degree of asymmetry, and map out the geographical distribution of the asymmetry for medium thick cloud variance ($\Delta\sigma^2$) and cloud count (ΔCC) in Figure 5 (January) and Figure 6 (August) to compare with mean cloud count and TB_C ($\bar{C}C$ and $\bar{TB}_C$).

[23] As shown in Figures 5d, 5h and Figures 6d, 6h, the anvils and cirrus associated with deep convection are well represented in the maps. Though the WF of the H_2O channels peak at 400 hPa, they become saturated in the presence of anvils. $\bar{TB}_C$ is slightly colder during daytime than nighttime in magnitude, but the geographic distributions are similar. The distribution of the cloud radiance variance $\bar{\sigma^2}$ also follows the $\bar{TB}_C$ climatology as expected because cloud inhomogeneity often occurs when deep convective clouds
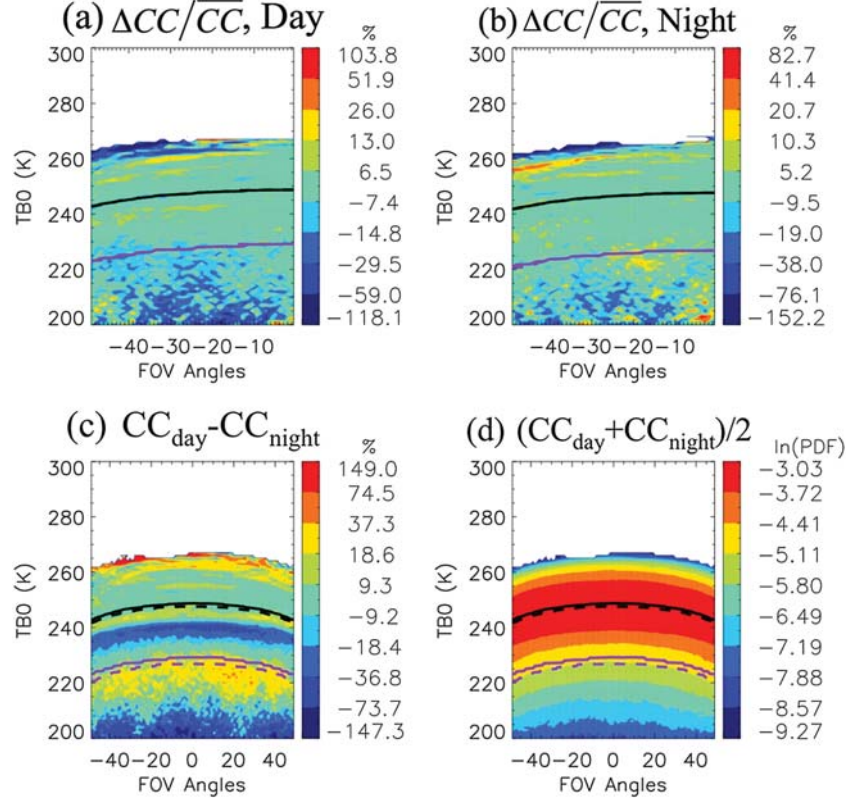
Figure 4. Mean January (2003–2011) equatorial difference of PDFs between pairwise west and east views during (a) daytime and (b) nighttime, between day and (c) night, and (d) the mean PDF as a function of view-angle and radiance. Black and purple solid (dashed) lines are the west-view (east-view) TB_{clr} and $TB_{clr} - 3\delta$ for Figure 4a (4b), and daytime (nighttime) for Figure 4c (4d). Negative (positive) view-angle always corresponds to west views (east views) in this paper. The equatorial belt is defined as [2.5°S, 2.5°N]. The PDFs are calculated from H_2O band **400 hPa** channels. Values less than **1/1000** of the maximum is written out.

are present. The January $\bar{\sigma^2}$ overland in daytime is ∼ 200% of that in nighttime (Figures 5c and 5g), whereas it is ∼ 130% in August (Figures 6c and 6g). Over ocean, the cloud variance exhibits a smaller day-night difference. August daytime variances in Central and North America are larger along the Rockies, while the center of enhanced variance moves to the ocean in nighttime, following closely to the $\bar{TB}_C$ pattern. Over land, deep convection begins to develop at local noon, anvils start to form, and there is large cloud inhomogeneity at this time. At midnight, the decaying stage of the convection, anvils have already smoothly spread out and start to dissipate, leading to a decrease of ma^2. Over ocean, the diurnal cycle amplitude for convection is much weaker [*Wylie and Woolf*, 2002; *Tian et al.*, 2004]. Therefore, the cloud $\bar{\sigma^2}$ over land has a greater diurnal difference despite the change of the cloud thickness. Because the oceanic convection is known to vary less within a day, the $\bar{\sigma^2}$ also maintains a relative stable value from ascending to descending orbits. A center of cold $\bar{TB}_C$ can be seen at south side of the Baja California Peninsula over the ocean. This might be associated with in situ generated cirrus clouds that are closely related to local water vapor and temperature perturbations [*Luo and Rossow*, 2004], as convection rarely develops over that region.

[24] Although most portions of the AIRS $\bar{\sigma^2}$ and $\bar{TB}_C$ patterns and day-night differences can be explained by the

diurnal variations of anvil clouds, the asymmetries are much more complicated, many features of which cannot be elucidated by a simple diurnal cycle. For example, at local mid-noon, both variance asymmetry ($\Delta\sigma^2$) and cloud count asymmetry (ΔCC) are predominantly negative, which means the west-view not only observes less anvil clouds than the east-view, but also finds more homogeneous clouds. The largest asymmetry occurs at convection-active regions over land, and over elevated terrains, e.g., Brazilian highlands and South Africa in January, Southern Rockies, southern Tibetan in August (Figure 10). The $\Delta\sigma^2$ collocates reasonably well with the ΔCC. At local midnight, both positive and negative differences exist and the amplitude becomes smaller. Although the daytime features are still somewhat resembled in the nighttime map, the nighttime patterns are much more chaotic and ambiguous.

[25] Lastly, we evaluate the angle dependence of TB_C, as this parameter is directly linked to cloudy-sky outgoing long-wave radiation (OLR). The $\bar{TB}_C$ in January for all clouds (i.e., $TB_C < TB_{clr} - 3\delta$) is shown in Figures 7a and 7c. As expected, the cloud is the coldest in the upward branch of the Hadley cell, corresponding to the most active convection. It is colder during daytime than nighttime. The coldest center leans to the east-view in daytime, and it is much more symmetric during nighttime. Interestingly, the secondary
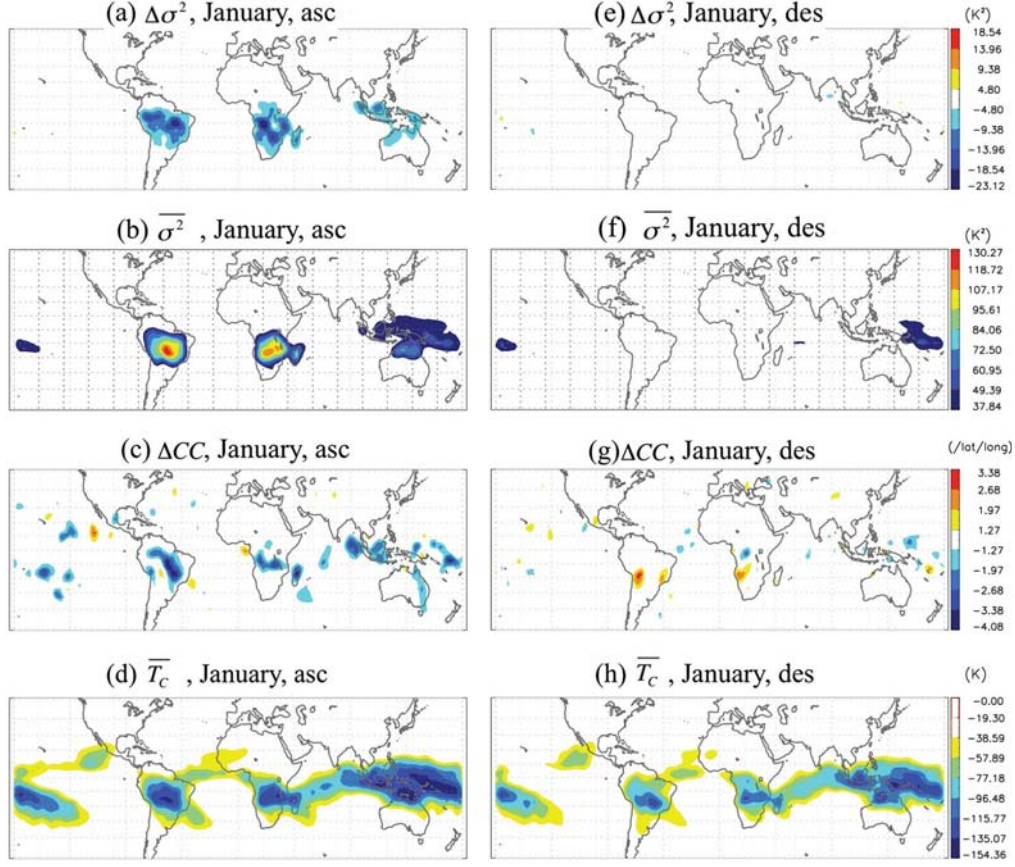
Figure 5. (a, e) Geographic distribution of variance asymmetry, (b, f) mean cloud variance, (c, g) cloud count asymmetry, and (d, h) mean cloud coldness averaged over January, 2003–2011 for AIRS H_2O 400 hPa channels for medium thick clouds. The left (right) panels are from ascending (descending) orbits. Values statistically insignificant (**95**% confidence level) are whiten out (same meaning hereafter).

cold belt near 5°N, corresponding to the in situ formed cirrus clouds near California and West Africa, also shows such an asymmetry feature, while they are not associated with local convection. By removing the limb-darkening effect using the equation $TB(\alpha) = TB_0 \ln[\cos(\alpha)]$, we can have a clue how much the observation deviates from the theory. The daytime gradient of residuals (Figure 7b) is quite consistent throughout the tropics and subtropics, and the separation occurs at around 20° east-view. It is interesting that in the winter hemisphere, the seesaw is totally opposite from that at the tropics, although the amplitude is much weaker. During nighttime, the amplitude of disagreement is much smaller, and the sign is inconsistent at different latitudes.

[26] As the diurnal cycle at various latitudes behaves differently in terms of the amplitude and the phase [*Yang and Slingo*, 2010], the surprisingly consistent seesaw characteristics during daytime is unlikely caused only by diurnal cycles of the clouds. Consequently, this figure implies that cloudy-sky OLR can be angle-dependent.

3.2. Microwave Humidity Sounder Asymmetry

[27] To quantify the relative importance of diurnal variations and other factors (e.g., structured clouds) in observed AIRS view-angle asymmetry, we analyze MHS data from NOAA-18 and NOAA-19, which has the same scan geometry to AIRS, except the satelliteorbital altitudes are slightly

different (Aqua altitude is 705 km, NOAA-18 is 854 km, and NOAA-19 is 870 km). During the month of August 2011, the same LST sampling is found between the ascending 37° east-view of NOAA-19 and the 37° west-view of NOAA-18 (1.9 and 13.9 LST, Figure 3). This coincidence provides us a unique opportunity to study the view-angle asymmetry because the cloud diurnal variation can be neglected if we compare the pair of 37° angles.

[28] The MHS has five microwave bands in which channel 3 and 4 ($183 \pm 1, \pm 3$ Hz) observe the middle troposphere (sounding channels). Unlike AMSUB, a similar instrument onboard earlier series of NOAA satellites, the MHS instrument has improved substantially to minimize the view-angle-dependent radio-frequency interference problem [*Buehler et al.*, 2005; *NOAA-18 briefing*, 2005]. We only present results from channel 3 (183 ± 1 Hz) here, which is most sensitive to -upper-middle troposphere clouds among all 5 channels. Although the MHS onboard NOAA-19 has some noise issue for Channel 3, the noise can be effectively removed by the 3δ cloud threshold, and show almost identical cloud climatologies between NOAA-18 and NOAA-19. At microwave spectra, these sounding channels can penetrate thick clouds and are less sensitive to thin clouds or clouds with small particles. Therefore, the cloud amount detected by MHS using 3δ method is much less than that observed by AIRS. Most of the AIRS anvils are not observed by MHS when the 3δ threshold is
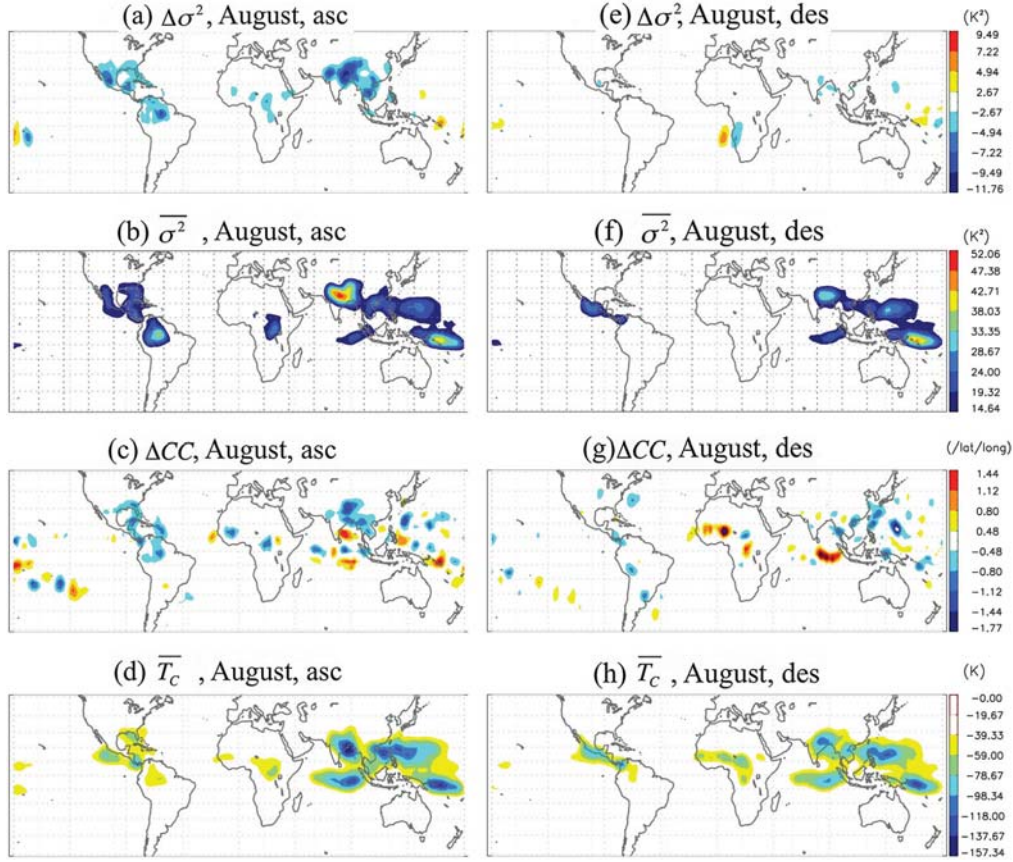
Figure 6. Same with Figure 5, except for August 2003–2010.

applied [*Berg et al.*, 1999], while the clouds detected by the 3δ method from MHS are mostly of deep convection type. Because the view-angle 37° from NOAA-18 west-view and NOAA-19 east-view have the same LST, we average the $\Delta\sigma^2$ parameter from angles between 32° and 42° for all clouds that are colder than $TB_{clr} - 3a$ to increase the sample size. In fact, the averages are largely insensitive to the width of selected view-angle range. MHS cloud occurrence climatology for the same month (not shown here) is in general agreement with AIRS at low latitudes, but the cloud distribution is more
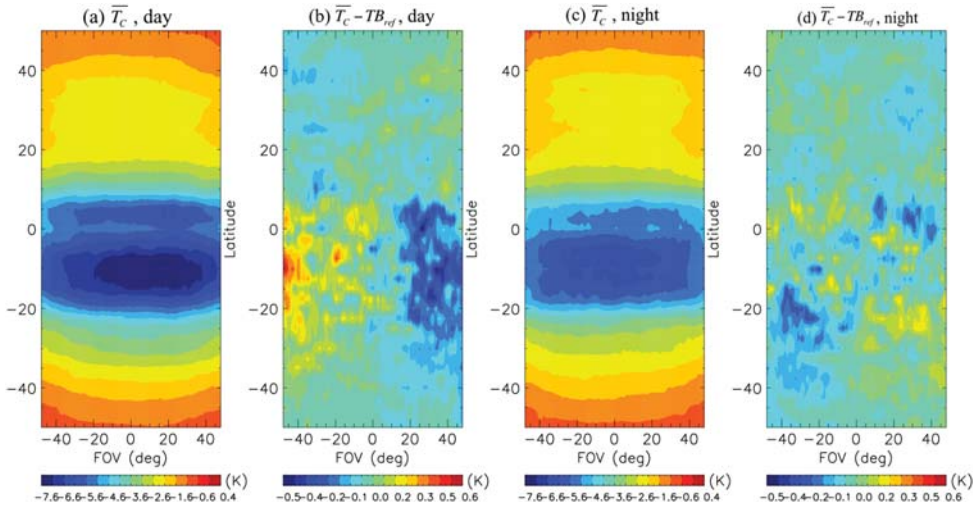
Figure 7. January averaged cloud induced TB_C for the (a) daytime and (c) nighttime as a function of view-angle and latitude. (b) and (d) Residuals from removing the limb-darkening effect of the mean. All clouds colder than $TB_{clr} - 3\delta$ are counted in. The colorbars for Figures 7a and 7c, 7b and 7d are the same, respectively.

confined to deep convective areas in MHS maps. At middle to high latitudes, MHS observes many clouds associated with jet streams that have relatively less occurrence frequency in AIRS 400 hPa H_2O channels compared to the tropics. Therefore, we anticipate the best agreement between MHS and AIRS results at the tropics and subtropics.

[29] The cloud variance asymmetry $\Delta\sigma^2$ and ΔTB_C from N18W to N19E (i.e., NOAA-18 west-view minus NOAA-19 east-view) are shown in Figures 8a and 8c for ascending only. Note that σ^2 and TB_C are averaged over all clouds. Both $\Delta\sigma^2$ (Figure 8a) and ΔCC (not shown) exhibit negative values over convectionaly active regions over land during daytime. The broad patterns are quite comparable with those observed by AIRS, although MHS maps are noisier than AIRS as we only have one month of data for MHS and the amount of clouds observed by MHS is much less than AIRS. The negative values in the MHS maps do not prefer high topography anymore, suggesting the diurnal variation plays an important role only on AIRS observed asymmetry over elevated terrain. During nighttime, the asymmetry in MHS radiance is weaker and less significant than that from daytime (not shown), consistent again with AIRS asymmetries.

[30] In this unique case, we can estimate the relative contributions from the diurnal and cloud variations (e.g., structured clouds) by computing the ratio of "N18W to N19E" $\Delta\sigma^2$ ("asymmetry component") and "N19W to N18E" $\Delta\sigma^2$ ("total" hereafter). The former is induced purely by structured cloud, and the latter should contain a diurnal contribution due to ~ 1.8 h local time difference and view-angle-dependent asymmetry due to structured clouds. The geographic distribution of $\Delta\sigma^2$ and ΔTB_C from the "total" (Figures 8b and 8d) exhibit highly coherent patterns with those from "asymmetry component" except the magnitudes are larger. By comparing Figure 8a with Figure 8b, we find $\sim 1/3$ of the $\Delta\sigma^2$ are induced from cloud variations rather than the diurnal variation at the tropics and the summer hemisphere subtropics. At higher latitudes, since most of the $\Delta\sigma^2$ values are statistically insignificant, the diurnal variation may dominate the "asymmetry component."

[31] The same ratio can be estimated for ΔTB_C from "asymmetry component" (Figure 8c) and the "total"

(Figure 8d), which gives a similar number of $1/3 - 2/3$. This ratio implies that a similar amount of daytime AIRS TB_C differences across a scan shown in Figure 7 are induced by cloud variations other than the diurnal variation. The possible candidates of these cloud variations include measurement errors, small sample size and time length, or physical factors such as structured clouds. If it is the cloud structures that accounts for the $1/3 - 2/3$ asymmetry in Figures 7b and 7d, it implies that cloudy-sky OLR could be directional, because OLR is proportional to TB^4, where TB here is the broadband averaged brightness temperature from long-wave band [*Ohring and Gruber*, 1984]. However, because ΔTB_C from the "asymmetry component" fails to pass the 95% significant test almost everywhere (note that the colors shown in Figure 8c and d are beyond one standard deviation only), we cannot conclude ΔTB_C have a significant view-angle-dependent asymmetry at this point.

[32] Microwave Humidity Sounder data provide a cross-validation of AIRS observed view-angle-dependent asymmetry. MHS and AIRS have similar viewing geometry, but the former does not blend with the diurnal signals during August 2011 between NOAA-18 west and NOAA-19 east views. Therefore, the asymmetry seen in the MHS measurements is very likely related to the view-angle sensitivity to tilted and banded cloud structures.

4. Discussions

4.1. Contributions From Diurnal Variations

[33] Contributions from the cloud diurnal cycle to scan-dependent cloudiness have been mentioned several times in the previous section. Upper-level clouds over landmasses usually develop together with local convection at local noon, become thick and more spread-out when convection intensifies in the late afternoon, and begin to dissipate in the late evening. In mountainous regions, the development stage may start earlier, and the amplitude of the diurnal cycle is often stronger [*Wylie and Woolf*, 2002], which is clearly reflected in Figure 10 where the maps are amplified for areas with large variance asymmetries with topography contoured on top. Because deep convection over ocean is typically weaker than that over land, the diurnal amplitude of
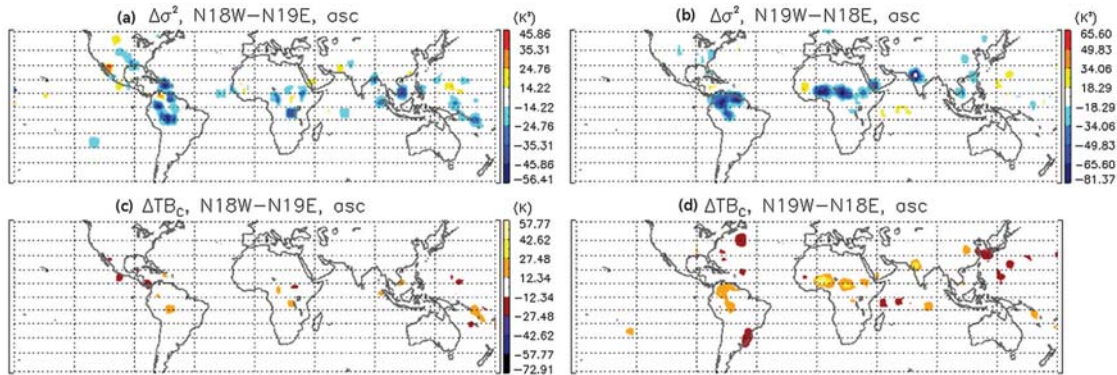
Figure 8. (a, b) Variance difference and TB_C (c, d) difference from MHS Channel 3 in August 2011. See text for the definitions of "N18W to N19E" and "N19W to N18E". Colored regions in Figures 8a and 8b pass the 95% significance test, while those in Figures 8c and 8d only pass the **68**% (one standard deviation) significance test.

upper-level clouds is weaker accordingly [*Tian et al.*, 2004]. The diurnal variations of upper-level clouds over various surface types can partly explain the negative difference between west and east views during daytime over land. As deep convection grows from 13 to 14 pm LST, anvil cloud counts increase accordingly, and the newly emerging anvils amplify the cloud inhomogeneity. This explains why the asymmetry tends to be larger in mountainous or high plateau regions.

[34] However, many of the observed asymmetric features cannot be completely explained by cloud diurnal variations. If the diurnal cycle was the only factor that controls the asymmetry, nighttime west-east view difference should have been weakly positive over land. However, the cloud occurrence frequency only increases about 10–20% from 13 to 14 pm LST based on ISCCP IR high cloud [*Wylie and Woolf*, 2002], while the asymmetry is about 15–60% of the "medium thick cloud" according to Figure 4a (bluish color below the purple line), the magnitude of which is comparable to the difference between daytime and night-time cloud counts (Figure 4c). Moreover, the diurnal variation does not explain the consistent 20° east-view sign shift for ΔT_B in Figure 7b nor the asymmetry in the MHS results from two NOAA satellites that have the same LST (Figure 8). Other causes must be taken into account to fully explain the AIRS and MHS observed cloud count and variance asymmetries.

4.2. Effects of Tilted and Organized Cloud Structures

[35] Tilted and banded cloud structures, as proposed by *Gong and Wu* [2011], produce an unavoidable effect that gives rise to the observed asymmetry, as illustrated in Figure 9. The radar reflectivity image is adapted from *Vincent et al.* [2011], showing the development/decay and advection of convection (i.e., leaving or incoming) over a tropical station. Above 10 km, the outflow at the convection top started to form anvils from 12 LST. At the beginning, convection was not strong, and the anvils tilted toward the left of the figure, equivalent to a westward tilt under a pre-dominant westward background wind. Such a tilted cloud structure would induce asymmetric cloudy radiances for AIRS and MHS instruments if it were simultaneously observed from different view-angles. During the decay/leaving of the old cell and development/incoming of the new cell, associated anvils formed a series of tilted and banded structures. This wavy pattern became more vertically aligned as convection enhanced. After convection reached its maximum ∼ 18 LST, the anvil height fell and so did the convection strength, with tilted cloud structures emerging again. Because AIRS radiances are a result of the convolution of radiation along the line-of-sight weighted by the AIRS WF, the east-view would observe optically thicker cloud layers and yield a larger radiance perturbation (i.e., radiance variation) than the west-view. The integration along AIRS west-view line-of-sight would encounter spaces in between cloud bands, and hence produce a smaller variation. Therefore, given a westward tilted series of banded structures, the AIRS west-view would detect a smaller cloud variation and cloud-induced radiance (i.e., smaller TB_C) than those from the east-view.

[36] If the above case is typical in the tropics and subtropics, the predominant negative values of $\Delta\sigma^2$ and ΔCC translate into a prevailingly westward tilt of the banded structures during day and night at the tropics and inthe summer hemisphere subtropics. These types of structures are common in radar images [e.g., *Marchand et al.*, 2008; *Gong and Wu*, 2011; *Vincent et al.*, 2011], and from model simulations [e.g., *Lane et al.*, 2001]. However, the anvil spread is often in the same direction with the diurnal cycle during daytime, resulting in a larger daytime asymmetry. Anvil decays together with convection at nighttime, which works against the diurnal cycle during nighttime, leading to noisy results at night. Because the IR channel can still penetrate through a thin cloud layer, AIRS indeed has the capability of capturing these structures.

[37] Looking into details of the areas with large variance asymmetries during daytime (Figure 10), we find that in all areas except the North American monsoon region (Figure 10d) the boundary layer wind shear (black arrows, $\rightarrow V_{700\ hPa} - \rightarrow V_{850\ hPa}$) is nearly always westward in those regions with large cloud asymmetries, while the upper-level wind shear (pink arrows, $\rightarrow V_{200\ hPa} - \rightarrow V_{400\ hPa}$) can go either eastward or westward. Wind data are from an ERA-Interim climatology. Ideally, one should integrate wind information in the vicinity of individual cloud. However, this type of data is not available nor accurate enough on a global sense for upper-level cloud. We can see a positive correlation from Figure 10 between lower-level wind shear and the direction of the tilt (except at the North America monsoon region in Figure 10d), while the relationship becomes vague with upper-level wind shear. The prevailing easterly wind in the tropics might cause the observed predominant westward tilted wavy structures, as the spread of the anvils naturally follows the horizontal wind direction. However, better correlation has been found with lower-level wind shear than that with the upper-level easterly wind in most of the places, indicating its importance on the tilt of the anvil structures. As pointed out by *Weisman and Rotunno* [2004], the tilted convective updrafts involve the vorticity competition between the lower-level wind shear and the precipitation-downdraft induced cold pool. At the early development stage of the convection, the cold pool is rather weak, and hence the convective cell tilts downshear of the lower-level wind. When the cold pool intensifies, the convective cell is more vertically tilted, and later on it tilts upshear [*Lane and Moncrieff*, 2010]. The entire life cycle of anvil development revealed in Figure 9 stresses its profound impact on the abundance of anvil cells. The large-area behavior of the anvils is likely rather inhomogeneous during the early developing stage, which occurs around local noon over land, and becomes quite homogeneous during the decaying stage, when deep convection stops to give birth to new anvils. The combined effect yields a coherent daytime westward tilt and a relative smaller nighttime tilt from the effects of both the tilted convective updrafts and the life-cycle of the anvils. Until further validated from other observations and from model simulations, we cannot argue which process plays a more important role. The AIRS results show that the windimpact on the anvil structures is much more complicated than the simple downstream spreading effect.

4.3. The Dominant Cloud Small Scales

[38] Cloud structures may possess different spatial and temporal characteristics compared with those of cloud as
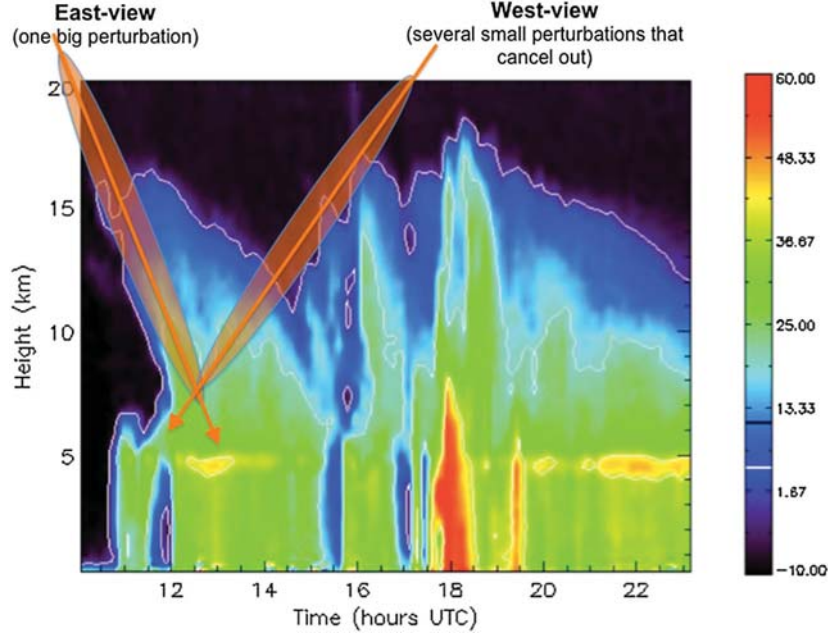
Figure 9. A schematic picture showing AIRS response to tilted and banded structures. The C-pol radar reflectivity image is adapted from *Vincent et al.* [2011] at Gunn Point, NT, Australia at 23 January 2006. See text for detailed illustrations. For MHS measurements, west-view (east-view) is equivalent to NOAA-18 and NOAA-19 for the daytime, and vice versa for the nighttime.

an entity. To investigate the dominant spatial/temporal scale of the cloud structures, we use fast Fourier transformation to decompose the residuals of the 90 AIRS cloud radiances within each scan in the way illustrated in equation (1). Figure 11 gives the August situation. Depending on how AIRS measurements were made spatially or temporally with respect to cloud variations, the dominant frequency has two interpretations: dominant spatial scale, or dominant period. In the regions where anvils are frequent, the dominant harmonic has a spatial scale of ~ 200 km or temporal period
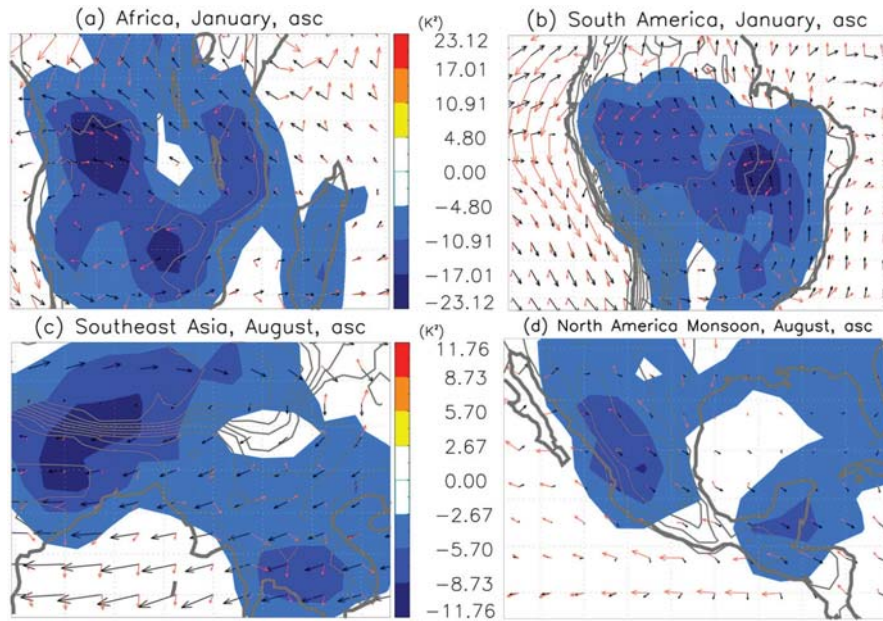
Figure 10. Amplification of the four regions with the largest variance asymmetries. Pink (black) arrows indicate the direction of the upper-troposphere (boundary layer) shear. Shear is defined as the lower-level wind subtracted from the upper-level wind (see text for the detailed definitions). Gray contours marked the topography.
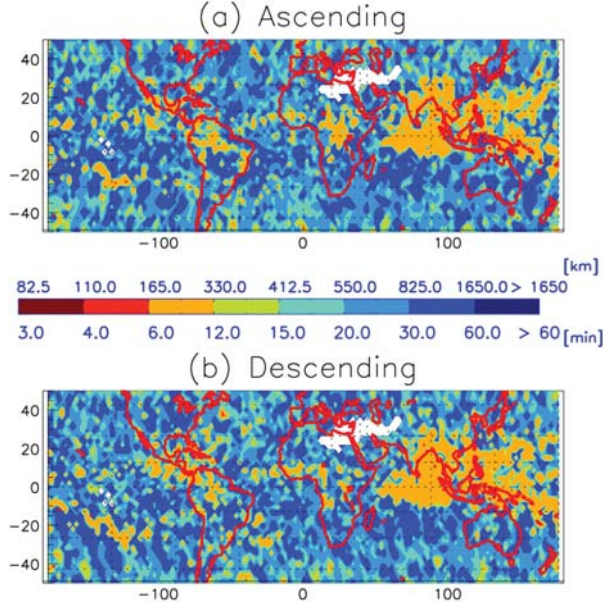
Figure 11. Dominant spatial scale or period of the asymmetry of cloud counts for August situation, which is calculated from the residual signal of AIRS H_2O 400 hPa channels and averaged over 2003–2010. Numbers above (below) the color bar corresponds to spatial scale (period). See text for details.

of ~ 10 min. It does not vary much between day and night, suggesting that this high-frequency signal is persistent all the time. The daytime covered areas seem to prefer elevated topography, which is more or less expected since the life-cycle of anvil clouds also modulates the strength of anvil cloud inhomogeneity. The small spatial scale/short temporal scale of cloud structure differentiates itself from cloud diurnal variations.

[39] The relatively high dominant frequency indicates that the tilted and banded cloud structures are spatially mesoscale, or oscillate on a fast pace without changing directions. The high frequency periodic feature is also discernible in the "medium thick cloud" in Figures 4a, 4b, and 4c. If it is a spatial signal, it may naturally correspond to the spatial scale of mesoscale convective systems (MCS) [cf. *Houze*, 2004] and the distance of anvil extent. If it is a temporal signal, it may be a consequence of some resonant frequency of the development of new convective cells [*Zehnder et al.*, 2007] or may involve wave-cloud interactions [*Lane and Zhang*, 2011]. The topic warrants further investigation.

5. Summary and Conclusions

[40] Following the initial work by *Gong and Wu* [2011] to study the angle-dependent tropical upper-troposphere cloud occurrence frequency, we extended the analysis to a wider latitude range (50°S, 50°N), and found that the view-angle-dependent asymmetry is of general existence for all anvils associated with deep convection. AIRS east-view tends to observe more anvil clouds than the west-view during the local noon, and this difference becomes less significant during local midnight. Moreover, this asymmetry is found to occur more often over land than over ocean. Over the landmasses, larger asymmetries are found above elevated terrain.

[41] Two leading causes were explored to better understand the observed view-angle dependency of AIRS cloudiness: local time difference among view angles, and the tilted and banded cloud structures. The local time difference can explain up to two-thirds of the observed zonal mean variance asymmetry in some regions, especially during the day over elevated terrain. In the regions with frequent anvil occurrence, the organized cloud structures are found to effectively induce the view-angle asymmetry in cloudiness and cloud variations, due to prevailing westward tilt at low to middle latitudes. The MHS sensors onboard NOAA-18 and NOAA-19 are used to examine the effect of structured clouds. Comparing cloud statistics at the same local time but opposite view-angles, we confirm the existence of view-angle-dependent cloudiness due to tilted and banded cloud structures. Although we do not have more collocated MHS data near AIRS local crossing time, the same method can be applied to other instruments with similar viewing geometries to increase the sample size, for example, between NPOESS Preparatory Project Cross-track Infrared Sounder and Aqua AIRS, between A series of polar orbiting satellites operated by European Organisation for the Exploitation of Meteorological Satellites and Infrared Atmospheric Sounding Interferometer, etc. One caveat of the cross-satellite comparison in this paper is that we neglect the potential impact of satellite orbital height differences, which create slightly different footprint sizes.

[42] The small-scale anvil structures have a dominant spatial (temporal) scale of ~ 200 km (10 min), corresponding to the typical MCS scale (convection overturning time scale or period from high-frequency gravity waves). They might be responsible for the tilted and banded anvil structures, which requires further evaluation from other independent observations and model simulations. The diurnal variation of anvil clouds plays a secondary role on modulating these structures. We have speculated two likely mechanisms for the tilted cloud structures: the wind-spreading effect, and the tilted convective updrafts. The hypothesis can be further tested with CloudSat radar measurements along the meridional direction, because it has simple vertical geometry, does not involve local time difference along the same scan, and the CloudSat radar profiles the vertical structures of different types of clouds, which can be integrated along any view angle for an ice water path (IWP). Some of our preliminary results from CloudSat indicate that deep convective and anvil clouds in the ITCZ are systematically tilted away from the equator, which are associated with the winds in the Hadley circulation.

[43] The analysis implemented in this study reveals the possible existence of angular heterogeneous radiation on top of the tilted band cloud structures. Our preliminary results imply that ENSO might impact the tilt and/or occurring frequency of these structures. The slantwise tilted structures would introduce further complexity in accurately calculating cloudy-sky shortwave and long-wave radiative forcings and cloud momentum fluxes. Quantification of these effects warrant further investigations.

Appendix A
List of AIRS Channels

Table A1. A List of Channel Numbers and Corresponding Noise Equivalent Differential Temperature (NEdT) That are Used in This Research. NEdT are Calculated Based on the Latest AIRS Channel Property Report.

Channel #	Frequency (μm)	Height (hPa)	NEdT (K)	band
156, 161, 162, 167, 169, 175	694.4, 695.8, 696.1, 697.4, 698.0, 699.7	200	0.30	CO_2
198, 207	706.1, 708.7	400	0.27	CO_2
294, 300	733.8, 735.7	800	0.34	CO_2
1614,1813	1419.7, 1577.0	300	0.15	H_2O
1719, 1800, 1815	1500.2, 1567.9, 1578.4	350	0.14	H_2O
1771, 1772, 1816	1547.9, 1548.6, 1579.1	400	0.16	H_2O
1573, 1634, 1821	1396.6, 1431.3, 1582.7	450	0.12	H_2O
1648, 1826, 1827	1439.5, 1586.3, 1587.0	500	0.16	H_2O
1561, 1627, 1651	1390.0, 1427.2, 1441.3	550	0.09	H_2O
1594, 1603	1408.3, 1413.4	600	0.10	H_2O
1518, 1519	1366.7, 1367.3	650	0.11	H_2O

References

Arakawa, A. (2004), The cumulus parameterization problem: past, present, and future, *J. Clim.*, *17*(13), 2493–2525.

Aumann, H. H., B. Steve, E. Denis, G. Steve, and G. Dave (2006), Three years of Atmospheric Infrared Sounder radiometric calibration validation using sea surface temperatures, *J. Geophys. Res.*, *1*, 11, doi:10.1029/2005JD006822.

Berg, W., J. J. Bates, and D. L. Jackson (1999), Analysis of upper-tropospheric water vapor brightness temperatures from SSM/T2, HIRS, and GMS-5 VISSR, *J. Atmos. Sci.*, *38*, 580–595.

Buehler, S. A., M. Kuvatov, and V. O. John (2005), Scan asymmetries in AMSU-B data, *Geophys. Res. Lett.*, *32*, L24810.

Campbell, G. G. (2004), View angle dependence of cloudiness and the trend in ISCCP cloudiness, Paper presented at the *13th Conference on Satellite Meteo. and Ocn*., Norfolk, VA. 23–29, Sep.

Cess, R. D., and co-authors (1990), Intercomparison and Interpretation of Climate Feedback Processes in 19 Atmospheric General Circulation Models, *J. Geophys. Res.*, *95*(D10), 16,601–16,615.

Cheng, C.-P., and R. A. Houze (1979), The distribution of convective and mesoscale precipitation in GATE radar echo patterns, *Mon. Wea. Rev. 107*, 1370–1381.

Diner, D. J., R. Davies, T. Vrnai, C. Moroney, C. Borel, S. A. W. Gerstl, and D. L. Nelson (1999), Multiangle Imaging SprectroRadiometer (MISR) level 2 top-of-atmosphere albedo algorithm theoretical basis, *JPL Rep. D-13401*, Revision D, 88 pp.

Evan, A. T., A. K. Heidinger, and D. J. Vimont (2007), Arguments against a physical long-term trend in global ISCCP cloud amounts, *Geophys. Res. Lett.*, *34*, L04701.

Ferrier, B. S., J. Simpson, and W.-K. Tao (1996), Factors responsible for precipitation efficiencies in midlatitude and tropical squall simulations, *Mon. Wea. Rev.*, *124*, 2100–2124.

Gong, J., and D. L. Wu (2011), View-angle dependent AIRS cloud radiances: Implications for tropical anvil structures, *Geophys. Res. Lett.*, doi:10.1029/2011GL047910.

Gu, Y., and K.-N. Liou (2006), Cirrus cloud horizontal and vertical inhomogeneity effects in a GCM, *Meteorol. Atmos. Phys.*, *91*, 223–235.

Houze, R. A., Jr. (2004), Mesoscale convective systems, *Rev. Geophys.*, *42*, RG4003, doi:10.1029/2004RG000150.

Kahn, B. H., A. Eldering, A. J. Braverman, E. J. Fetzer, J. H. Jiang, E. Fishbein, and D. L. Wu (2007), Toward the characterization of upper tropospheric clouds using atmospheric infrared sounder and microwave limb sounder observations, *J. Geophys. Res.*, *112*, doi:10.1029/2006JD007336.

Kang, I.-S., D.-Y. Kim, and J.-S. Kug (2010), Mechanism for northward propagation of boreal summer intraseasonal oscillation: convective momentum transport, *Geophys. Res. Lett.*, *37*, doi:10.1029/2010GL045072.

Kikuchi, K., T. Aoyama, Y. Asuma, and T. Taniguchi (1994), Roughness of cloud top surfaces of winter stratocumulus clouds over the ocean - - preliminary investigations on cloud and radiation (1994), *J. Fac. Sci.*, *9*, 381–403.

Lane, T. P., M. J. Reeder, and T. L. Clark (2001), Numerical modeling of gravity wave generation by deep tropical convection, *J. Atmos. Sci.*, *58*, 1249–1274.

Lane, T. P., and M. W. Moncrieff (2010), Characterization of momentum transport associated with organized moist convection and gravity waves, *J. Atmos. Sci.*, *67*, 3208–3225.

Lane, T. P., and F. Q. Zhang (2011), Coupling between Gravity Waves and Tropical Convection at Mesoscales, *J. Atmos. Sci.*, *68*, 2582–2598.

Li, J., and Q. Fu (2000), Absorption approximation with scattering effect for infrared radiation, *J. Atmos. Sci.*, *57*, 2905–2914.

Lienesch, J. H., and D. Q. Wark (1967), Infrared limb darkening of the Earth from statistical analysis of TIROS data, *J. Appl. Meteor.*, *6*, 674–682.

Liu, C., and E. J. Zipser (2008), Diurnal cycles of precipitation, clouds, and lightning in the tropics from 9 years of TRMM observations, *Geophys. Res. Lett.*, *35*, L04819, doi:10.1029/2007GL032437.

Luo, Z. Z., and W. B. Rossow (2004), Characterizing tropical cirrus life cycle, evolution, and interaction with upper-tropospheric water vapor using Lagrangian trajectory analysis of satellite observations, *J. Clim.*, *17*, 4541–4563.

McNally, A. P., P. D. Watts, J. A. Smith, R. Engelen, G. A. Kelly, J. N. Thepaut, and M. Matricardi (2006), The assimilation of AIRS radiance data at ECMWF, *Q. J. R. Meteorol. Soc.132*, 935–957.

Maddux, B. C., S. A. Ackerman, and S. Platnick (2010), Viewing geometry dependencies in MODIS cloud products, *J. Atmos. Oceanic Tech.*, *27*(9), 1519–1528.

Marchand, R., G. G. Mace, T. Ackerman, and G. Stephens (2008), Hydrometeor Detection Using CloudsatÑAn Earth-Orbiting 94-GHz Cloud Radar, *J. Atmos. Oceanic Technol.*, *25*, 519–533.

Minnis, P., D. F. Young, and E. F. Harrison (1991), Examination of the relationship between outgoing infrared window and total longwave fluxes using satellite data, *J. Clim.*, *4*, 1114–1133.

NOAA-18 Instrument CalVal Briefing - June20-24 (2005), http://www.star.nesdis.noaa.gov/smcd/spb/n18calval/briefing.html.

OÕHirok, W., and C. Gautier (1998), A Three-dimensional radiative transfer model to investigate the solar radiation within a cloudy atmosphere. Part II: spectral effects, *J. Atmos. Sci.*, *55*, 3065–3076.

Ohring, G., and A. Gruber (1984), Satellite determination of the relationship between total longwave radiation flux and infrared window radiance, *J. Climate Appl. Meteor.*, *23*, 416–425.

Ramaswamy, V., and V. Ramanathan (1989), Solar Absorption by Cirrus Clouds and the Maintenance of the Tropical Upper Troposphere Thermal Structure, *J. Atmos. Sci.*, *46*, 2293–2310.

Soden, B. J., and F. P. Bretherton (1993), Upper tropospheric relative humidity from the GOES 6.7µm channel: method and climatology for July 1987, *J. Geophys. Res.*, *98*, 16669–16688.

Su, H., J. H. Jiang, G. L. Stephens, D. G. Vane, and N. J. Livesey (2009), Radiative effects of upper tropospheric clouds observed by Aura MLS and CloudSat, *Geophys. Res. Lett.*, *36*, L09815.

Tian, B.-J., B. J. Soden, and X.-Q. Wu (2004), Diurnal cycle of convection, clouds, and water vapor in the tropical upper troposphere: Satellite versus a general circulation model, *J. Geophys. Res. 109*, doi:10.1029/2003JD004117.

Varnai, T., and A. Marshak (2002), Observations of three-dimensional radiative effects that influence MODIS cloud optical thickness retrievals, *J. Atmos. Sci.*, *59*, 1607–1618.

Vincent, R., J. A. Alexander, S. Kovalam, A. Mackinnon, et al. (2011), An integrated study of gravity wave generation and propagation, *AGU Chapman Conference on Atmospheric Gravity Waves and Their Effects on General Circulation and Climate*, February 28 - March 4, 2011.

Weisman, M. L., and R. Rotunno (2004), A theory for strong long-lived squall lines revisted, *J. Atmos. Sci.*, *61*, 361–382.

Weng, F., L. Zhao, R. Ferraro, G. Poe, X. Li, and N. Grody (2003), Advanced microwave sounding unit cloud and previpitation algorithms, *Rdio Sci.*, *38*(4), MAR 33–1.

Wu, D. L., W. G. Read, A. E. Dessler, S. C. Sherwood, and J. H. Jiang (2005), UARS/MLS cloud ice measurements: implications for H2O transport near the tropopause, *J. Atmos. Sci.*, *62*, 518–530.

Wylie, D. P., and H. M. Woolf (2002), The diurnal cycle of upper-tropospheric clouds measured by GOES-VAS and the ISCCP, *Mon. Wea. Rev.*, *130*, 171–179.

Yang, G.-Y., and J. Slingo (2010), The diurnal cycle in the tropics, *Mon. Wea. Rev.*, *129*, 784–801.

Yuan, J., R. A. Houze, and A. J. Heymsfield (2011) Vertical Structures of Anvil Clouds of Tropical Mesoscale Convective Systems Observed by CloudSat., *J. Atmos. Sci.*, *68*, 1653–1674.

Zehnder, J. A., J. Hu, and A. Razdan (2007), A Stereo Photogrammetric Technique Applied to Orographic Convection, *Mon. Wea. Rev.*, *135*, 2265–2277.

Zhang, G. J., and X. Q. Wu (2003), Convective momentum transport and perturbation pressure field from a cloud-resolving model simulation, *J. Atmos. Sci.*, *60*, 1120–1139.